Measurement quality metrics for rapid laser range scanning

MacKinnon, David; Blais, François; Aitken, Victor

Publisher's version / Version de l'éditeur:
https://doi.org/10.1117/1.3267094
SPIE Journal of Electronic Imaging, 19, 1, pp. 0111004-1-0111004-12, 2010-08-01

Measurement quality metrics for rapid laser range scanning

David MacKinnon
François Blais
National Research Council of Canada
Institute for Information Technology
David.MacKinnon@nrc-cnrc.gc.ca

Victor Aitken
Carleton University
Department of Systems and Computer Engineering
Canada

Abstract. *Quality metrics quantify by how much some aspect of a measurement deviates from a predefined standard. Measurement quality evaluations of laser range scanner data are used to perform range image registration, merging measurements, and view planning. We develop a scanning method that uses laser range scanner quality metrics to both reduce the time required to obtain a complete range image from a single viewpoint and the number of measurements obtained during the scanning process. This approach requires a laser range scanner capable of varying both the area and sampling density of individual scans, but can be combined with view planning methods to reduce the total time required to obtain a complete surface map of an object. Several new quality metrics are introduced: outlier, resolvability, planarity, integration, return, and enclosed quality metrics. These metrics are used as part of a quality-based merge method, referred to here as a quality-weighted modified Kalman minimum variance (weighted-MKMV) estimation method. Experimental evidence is presented confirming that this approach can significantly reduce the total scanning time. This approach could be particularly useful for rapidly generating CAD models of real-world objects.* © *2010 SPIE and IS&T.*
[DOI: 10.1117/1.3267094]

1 Introduction

Measurement quality evaluations are becoming increasingly important in laser range imaging for a variety of applications; however, a recent survey[1] of laser range scanner quality metrics identified several unresolved issues with regard to quantifying laser range scanner quality measurements. According to the survey, no quality metric exists to address the affect on laser range scanner measurement quality of beam footprint motion during acquisition, measurement resolution, or the presence of nonreturn measurements. A series of new quality metrics are presented in this work to address these issues, as well as some that were not identified in Ref. 1: surface planarity and the effect of data processing on measurement quality.

Measurement quality metrics have rarely been used to drive the measurement acquisition process. Sequeira *et al.*[2] used quality metrics to more effectively merge overlapping range images and as part of the view planning process. Callieri *et al.*[3] used quality metrics for view planning as part of a multistage approach. This approach, first developed by Scott, Roth, and Rivest[4] for small-volume scanning, involved acquiring an initial low-density scan which was then used to plan a series of viewpoints from which to acquire high-density scans.

A multistage method is presented in this work in which quality metrics are used to minimize the time required to acquire a range image from a single viewpoint while maximizing the overall quality of the final range image. This is accomplished by scanning only the areas of the total field of view where it is likely that a high-density scan would improve the final range image obtained from that viewpoint. Experiments using this method demonstrate that both the time required to acquire a high-quality range image and the total number of measurements acquired can be significantly reduced when compared to that required to acquire a single high-density range image. Figure 1 shows the setup used to perform all experiments. Reducing the number of measurements can reduce postprocessing time and, by extension, reduce the time between initial acquisition and fi-

Fig. 1 Experimental setup.

Paper 09051SSR received Apr. 21, 2009; revised manuscript received Jun. 18, 2009; accepted for publication Jul. 22, 2009; published online Jan. 7, 2010.

1017-9909/2010/19(1)/011004/12/$25.00 © 2010 SPIE and IS&T.

nal model generation. This scanning method is well suited for either fully automated scanning systems or systems that guide a minimally trained operator.

2 Range Measurement Quality Metrics

The quality of a laser range scanner measurement depends on measurement uncertainty and measurement resolution; however, spatial uncertainty is also strongly affected by other environmental factors such as the type of surface material,[5] surface reflectivity,[6] distance to the surface,[6,7] and incidence angle.[8] The purpose of a quality metric is to quantify some aspect of the quality of a laser range scanner measurement with respect to some previously established benchmark. No attempt has been made to establish optimal benchmark values for the quality metrics used in this work, because benchmark values are application and scanner specific so must be established on a case-by-case basis. The benchmark values used in this work have been obtained for the laser range scanner used in this experiment for the purpose of minimizing model acquisition time.

In this section, we introduce a series of quality metrics $c_i^{\text{metric}} \in [0,1]$ for laser range scanner measurements. All quality metrics presented use the range $c_i^{\text{metric}}=1$ (ideal quality) to $c_i^{\text{metric}}=0$ (unacceptable quality), where the term "metric" refers to any quality metric presented here. In some cases, the quality metric associated with a measurement $\mathbf{p}_i$ is defined relative to its neighborhood in the range image. The neighborhood $N(\mathbf{p}_i)$ of a range image measurement $\mathbf{p}_i$ is broadly defined as a set of K_i measurements $\{\mathbf{p}_j,\ldots,\mathbf{p}_j+K_i-1\}$ that are neighbors of $\mathbf{p}_i$ according to some previously defined neighborhood criteria. The neighborhood criteria used to define $N(\mathbf{p}_i)$ depends on how the range image is constructed; for example, $N(\mathbf{p}_i)$ for a range image consisting of a regular grid of measurements can be defined as all range image measurements immediately adjacent to $\mathbf{p}_i$. In this case, measurements on the interior of this range image would have exactly $K_i=8$ neighbors, while those on the boundary would have either $K_i=3$ or $K_i=6$ neighbors.

2.1 *Return Quality Metric*

The return quality metric c_i^{return} indicates whether the measurement has a valid range and intensity value. A measurement should ideally have a valid range and intensity value and would be assigned $c_i^{\text{return}}=1$; otherwise, it would be assigned $c_i^{\text{return}}=0$. Measurements in which $c_i^{\text{return}}=1$ are defined as return measurements because the laser range scanner measurement arises from a return signal that could be converted by the scanning system into a range and intensity value. Measurements in which $c_i^{\text{return}}=0$ are defined as nonreturn measurements, and can be the result of either insufficient return signal intensity or a return signal that saturates the detector. In the case of time-of-flight systems, it can also mean that no return signal was detected during the ambiguity interval.[7] All other quality metrics describing $\mathbf{p}_i$ are assigned $c_i^{\text{metric}}=0$ if $c_i^{\text{return}}=0$.

2.2 *Enclosed Quality Metric*

In some situations, reported values arise from neighborhood-based procedures. For example, some of the metrics presented here, as well as many data processing procedures, use all the neighbors of a measurement. If some of those neighbors are nonreturn measurements, or if the measurement is on the boundary of a range image, then the reported values may be based on an insufficient or asymmetric dataset. A measurement is defined as an enclosed measurement if all neighbors of the measurement are return measurements and the measurement is not on the boundary of the range image. If a measurement is an enclosed measurement, then it is assigned $c_i^{\text{enc}}=1$; otherwise, it is assigned $c_i^{\text{enc}}=0$ and is defined as a nonenclosed measurement.[9,10]

2.3 *Outlier Quality Metric*

The outlier quality metric c_i^{out} represents the effect of data processing on the quality of range and intensity measurements. Data processing involves activities like smoothing that are intended to improve the range image by reducing the effect of measurement noise; however, data processing can, and often does, change the measurement value v_i associated with $\mathbf{p}_i$. In some cases, this change can be significantly greater than what would be expected based on experimentally determined measurement uncertainty s_V. If $\Delta v_i=|v_i^{\text{raw}}-v_i^{\text{processed}}|$, where v_i^{raw} is the original (raw data) measurement and $v_i^{\text{processed}}$ is the processed measurement, is greater than the two-tailed error margin v_i^{err},[11] then $\mathbf{p}_i$ has less than ideal quality.[9,10]

The quality metric c_i^{out} is the minimum, or worst case, of the range outlier quality metric $c_{i,R}^{\text{out}}$ and the intensity outlier quality metric $c_{i,I}^{\text{out}}$. The quality metric c_i^{out} is found using

$$c_i^{\text{out}}=\min\{c_{i,R}^{\text{out}},c_{i,I}^{\text{out}}\}, \tag{1}$$

where

$$c_{i,R}^{\text{out}}=\begin{cases}1 & \Delta R_i \leqslant R_i^{\text{err}} \\ \dfrac{R_i^{\text{err}}}{\Delta R_i} & \text{otherwise}\end{cases}, \tag{2}$$

and

$$c_{i,I}^{\text{out}}=\begin{cases}1 & \Delta I_i \leqslant I_i^{\text{err}} \\ \dfrac{I_i^{\text{err}}}{\Delta I_i} & \text{otherwise}\end{cases}, \tag{3}$$

are the range $(v=R)$ and intensity $(v=I)$ outlier quality metrics respectively.[9,10] A simple ratio model was employed to make it easy for a minimally trained operator to interpret the graphical representation of c_i^{out}. This metric is dependent on the type of data processing that is used, so when stating the outlier quality, it must be made clear what data processing procedures separate the raw and processed results. Data processing procedures—like averaging and median filtering—are neighborhood-based procedures, so the quality of c_i^{out} can be assessed using c_i^{enc}.

2.4 *Planarity Quality Metric*

The planarity quality metric c_i^{plane} indicates whether the surface within $N(\mathbf{p}_i)$ is locally planar, based on whether $\mathbf{p}_i$ is contained within a locally planar neighborhood.[12] Measurements arising from planar surfaces are considered to be of ideal quality because there are no discontinuities to intro-

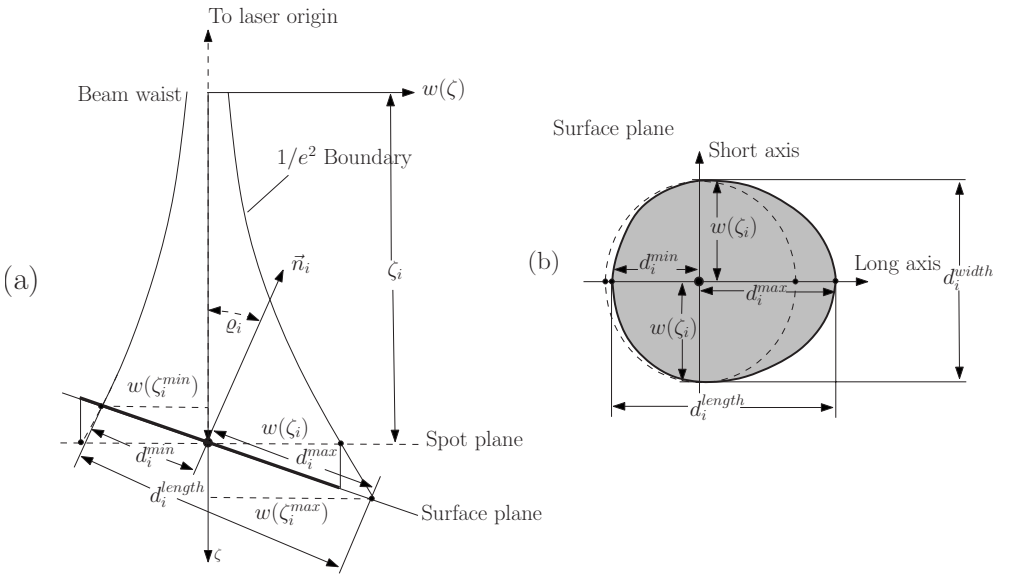

Fig. 2 Beam intersection with an angled planar surface results in an oval beam footprint with length d_i^{length} and width $2w(\zeta_i)$, where ζ_i is the distance from the surface to the beam waist along the beam axis. (a) Side view with short axis directed outward from the page, and (b) top view with normal directed outward from the page.

duce measurement error, so they are assigned $c_i^{\text{plane}}=1$; otherwise, they are assigned $c_i^{\text{plane}}=0$. Measurements in which $c_i^{\text{plane}}=1$ are defined as planar measurements, meaning that the measurement arises from a planar surface, and measurements in which $c_i^{\text{plane}}=0$ are defined as nonplanar measurements.[9,10] The metric c_i^{plane} is a neighborhood-based metric, so its quality can be assessed using c_i^{enc}.

2.5 *Resolvability Quality Metric*

The resolvability quality metric c_i^{res} is used to identify regions that cannot be resolved at the target surface resolution Δx to within a margin of error given the current scanner viewpoint. The beam should ideally intersect a surface close enough to the scanner, and with a sufficiently low surface orientation so that the width of the beam footprint is less than Δx. If it is likely that the width of the beam footprint is too large to resolve surface details to at least Δx, then any measurement arising from this surface is considered to be of unacceptable quality. The quality metric c_i^{res} is found by

$$c_i^{\text{res}}=\begin{cases}1 & d_i^{\text{length}}\leqslant d_i^{\text{up}}\\ \dfrac{d_i^{\text{up}}-d_i^{\text{width}}}{d_i^{\text{length}}-d_i^{\text{width}}} & d_i^{\text{width}}<d_i^{\text{up}}<d_i^{\text{length}}\\ 0 & d_i^{\text{up}}\leqslant d_i^{\text{width}}\end{cases}, \tag{4}$$

where d_i^{width} is the width of the short axis of the beam footprint, d_i^{length} is the length of the long axis of the beam footprint, and $d_i^{\text{up}}=\Delta x+2d_i^{\text{err}}$ is the target surface resolution with an error margin based on the measurement rotational uncertainty.[9,10] All three terms are illustrated in Fig. 2. The length of the long axis of the beam footprint is found by $d_i^{\text{length}}=d_i^{\text{max}}+d_i^{\text{min}}$, the sum of components of the long axis. For a Gaussian beam, these components are found using

$$\{d_i^{\text{min}},d_i^{\text{max}}\}=\left|\frac{-K_{i,2}\pm\sqrt{K_{i,2}^2-4K_{i,1}K_{i,3}}}{2K_{i,1}}\right|, \tag{5}$$

where

$$K_{i,1}=[w(0)\sin(\rho_i)]^2-[\zeta_0\cos(\rho_i)]^2,$$

$$K_{i,2}=2\zeta_i w^2(0)\sin(\rho_i),$$

$$K_{i,3}=[w(0)\zeta_0]^2+[w(0)\zeta_i]^2, \tag{6}$$

and are illustrated in Fig. 2.[9,10] The $w(0)$ term represents the predicted radius of the beam waist, ζ_i is the radial distance from the beam waist, ρ_i is the angle between the surface normal estimate $\vec{n}_i$ and the laser path $\vec{r}_i$, and ζ_0 is the depth of focus.[13] The derivation of Eq. (5) can be found in Appendix A in Sec. 6 and applies only to a Gaussian beam being transmitted through a medium with negligible effect on beam spread.[14,15] The error term d_i^{err} is added to the surface distance from the beam footprint center to the beam footprint edge to ensure that the scanner is close enough to the surface to resolve features to at least Δx with a margin of error. To simplify the equation, the surface is assumed to be locally planar, so the quality of c_i^{res} can be assessed using c_i^{plane}. This error term is found using

$$d_i^{\text{err}}=\frac{R\sin(\theta_{\text{err}})}{\cos(\gamma_i)-\sin(\gamma_i)\sin(\theta_{\text{err}})}, \tag{7}$$

in which the rotational error term θ_{err} is defined as

$$\theta_{\text{err}}=[\chi^2(1,\alpha)(\max\{s_\theta^2,s_\phi^2\})]^{1/2}, \tag{8}$$

where $\chi^2(1,\alpha)$ is the chi-squared statistic with significance level α and one degree of freedom, and s_θ and s_ϕ are the

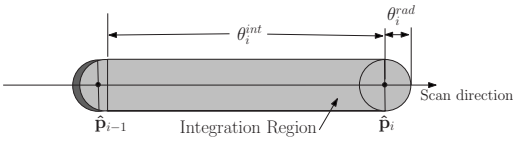

Fig. 3 The range measurement uncertainty of laser range scanners is reduced by integrating $\hat{\mathbf{p}}_i$ with instantaneous beam footprint radius θ_i^{rad} over a distance θ_i^{int}. Integration consists of combining multiple samples into a single measurement.

experimentally determined horizontal (θ) and vertical (ϕ) rotational uncertainties. The θ_{err} term represents the maximum rotational distance between two points, in this case the center of one beam footprint and the edge of its neighboring beam footprint, such that they can still be considered likely to represent the same point to within a confidence level determined by α, given the expected rotational uncertainty of the scanner.[9,10]

All measurements with $c_i^{\text{res}}=0$ are defined as unresolvable measurements, meaning that surface features cannot be resolved at Δx for these measurements: those with $1>c_i^{\text{res}}>0$ are defined as resolvable measurements, and measurements with $c_i^{\text{res}}=1$ are defined as completely resolvable measurements.[9,10] The range (c_i^{range}) and orientation (c_i^{orient}) quality metrics, discussed in Sec. 2.7, complement c_i^{res} when defining the bounds of the scannable region. The quality metric c_i^{plane} is a neighborhood-based metric because it is based on an estimate of the surface normal, so its quality can be assessed using c_i^{enc}.

2.6 *Blur Quality Metric*

The blur quality metric c_i^{blur} represents the blurring of a laser range scanner measurement as a result of the motion of the beam footprint during acquisition. Measurement uncertainty in triangulation laser range scanners is typically reduced by integrating a single measurement over several intensity samples to counter the effect of speckle noise,[16,17] as illustrated in Fig. 3. Blurring can also occur in continuous-wave scanners, because the beam footprint is moving during acquisition of the reflected beam peak, but pulse time-of-flight scanners use short pulse lengths, so the likelihood of measurement blurring is minimal unless multipulse integration is employed to reduce measurement uncertainty. Ideally, the integration distance should be zero to avoid measurement blurring.

The blur quality metric c_i^{blur} is obtained using

$$c_i^{\text{blur}}=\begin{cases}1 & \theta_i^{\text{int}}=0\\ \dfrac{\theta_i^{\text{rad}}}{\theta_i^{\text{rad}}+\theta_i^{\text{int}}} & \text{otherwise}\end{cases}, \tag{9}$$

where θ_i^{int} is the rotational distance between $\mathbf{p}_i$ and the measurement $\mathbf{p}_{i-1}$ that immediately preceded it in the scan line, and θ_i^{rad} is the radius of the beam footprint in rotational units. The blur metric is assigned $c_i^{\text{blur}}=0$ if $\mathbf{p}_{i-1}$ is not in the same scan line or if $\mathbf{p}_{i-1}$ is a nonreturn measurement, because there is no way to assess the blur quality without a measurement preceding it in the scan line.[9,10] A simple ratio model was employed to make it easy for a minimally trained operator to interpret the graphical representation of c_i^{blur}.

2.7 *Additional Quality Metrics*

The orientation quality metric c_i^{orient} is defined as

$$c_i^{\text{orient}}=\begin{cases}0 & \vec{n}_i^T\hat{\mathbf{x}}_i\leqslant\vec{n}_{\max}^T\hat{\mathbf{x}}_i\\ \dfrac{(\vec{n}_i-\vec{n}_{\max})^T\hat{\mathbf{x}}_i}{\hat{R}_i-\vec{n}_{\max}^T\hat{\mathbf{x}}_i} & \text{otherwise}\end{cases}, \tag{10}$$

where $\hat{\mathbf{x}}_i$ is a measurement located a distance $\hat{R}_i$ radially from the viewpoint, $\vec{n}_i$ is the unit normal to the surface at $\hat{\mathbf{x}}_i$, and $\vec{n}_{\max}$ is the unit normal for a surface that is oriented $\rho_{\max}$, the user-defined maximum acceptable surface orientation, with respect to the laser path. Measurements with $c_i^{\text{orient}}=0$ are classified as angled measurements and arise from surfaces that are so highly angled that measurements from them would be discarded during postprocessing. Measurements with $c_i^{\text{orient}}>0$ are defined as nonangled measurements.[9,10] Surface orientation is a commonly used quality metric;[18–23] however, previous versions of this metric did not employ a maximum acceptable surface orientation as part of the metric. The metric c_i^{orient} is a neighborhood-based metric because it is based on an estimate of the surface normal, so its quality can be assessed using c_i^{enc}.

The reflectivity quality metric c_i^{ref} is defined by

$$c_i^{\text{ref}}=\begin{cases}0 & \rho_i\geqslant\rho_{\max}\\ \dfrac{\rho_{\max}-\rho_i}{\rho_{\max}-1} & \rho_{\max}>\rho_i>1\\ 1 & \rho_i=1\\ \dfrac{\rho_i-\rho_{\min}}{1-\rho_{\min}} & \rho_{\min}<\rho_i<1\\ 0 & \rho_i\leqslant\rho_{\min}\end{cases}, \tag{11}$$

where $\rho_{\min}$ and $\rho_{\max}$ are user-defined bounds on the acceptable reflectivity of the surface, and ρ_i is the surface reflectivity relative to a reference surface. The surface reflectivity is found using

$$\rho_i=\frac{I_i}{I(R_i)}, \tag{12}$$

where I_i is the return signal intensity and $I(R_i)$ is the model-based return signal intensity obtained during calibration. The model-based return signal intensity represents the intensity of the surface used to obtain the models for range and rotational uncertainty.[9,10] Fiocco *et al.*[20] had previously defined a reflectivity quality metric as a binary quality metric; however, their approach reduced the generalizability of the metric.

The range quality metric c_i^{range} is defined by

$$c_i^{\text{range}} = \begin{cases} 0 & R_i \geqslant R_{\max} \\ \dfrac{R_{\max} - R_i}{R_{\max} - D(R_i, \theta_i, \phi_i)} & R_{\max} > R_i > R_{\text{spot}}(\theta_i, \phi_i) \\ 1 & R_i = R_{\text{spot}}(\theta_i, \phi_i) \\ \dfrac{R_i - R_{\min}}{D(R_i, \theta_i, \phi_i) - R_{\min}} & R_{\min} < Ri < R_{\text{spot}}(\theta_i, \phi_i) \\ 0 & R_i \leqslant R_{\min} \end{cases}, \tag{13}$$

where $R_{\max}$ is the user-defined maximum acceptable range measurement, $R_{\min}$ is the user-defined minimum acceptable range measurement, and $R_{\text{spot}}(\theta_i, \phi_i)$ is the distance to the beam waist. The beam diameter orthogonal to the beam axis is smallest at the beam waist, so this represents the ideal distance to any surface in the total field of view. Fiocco *et al.*[20] also defined a distance quality metric based on the minimum and maximum range limits, while Sequeira *et al.*[2,18] applied a weighting factor to the range measurement to obtain a quality metric. Measurements with $c_i^{\text{range}}=0$ are defined as out-of-range measurements.

The sampling quality metric c_i^{sample} represents the likelihood that a scan is sufficiently dense to ensure that features at the desired surface resolution will be detected. The surface distance d_i^{far} from $\mathbf{p}_i$ to the most distant neighbor $\mathbf{p}_j^{\max} \in N(\mathbf{p}_i)$ should ideally be within the beam footprint; however, rotational uncertainty makes it impossible to know precisely where the $1/e^2$ boundary intersects the surface. The quality metric c_i^{sample} is defined as a fuzzy transition between most and least probable surface distance to where the $1/e^2$ boundary would intersect the surface. The sampling quality metric is found by

$$c_i^{\text{sample}} = \begin{cases} 0 & d_i^{\text{up}} \leqslant d_i^{\text{far}} \\ 1 - \dfrac{d_i^{\text{far}} - d_i^{\text{low}}}{2d_i^{\text{err}}} & d_i^{\text{low}} < d_i^{\text{far}} < d_i^{\text{up}} \\ 1 & d_i^{\text{far}} \leqslant d_i^{\text{low}} \end{cases}, \tag{14}$$

where $\{d_i^{\text{low}} = \Delta x - 2d_i^{\text{err}},\ d_i^{\text{up}} = \Delta x + 2d_i^{\text{err}}\}$ represent the α-bounds on the target resolution. To simplify the equation, the surface is assumed to be locally planar so the quality of c_i^{sample} can be assessed using c_i^{plane}. According to the Shannon-Nyquist sampling theorem, the distance between samples must be less than half the smallest feature size to be resolved; otherwise, aliasing distortion occurs.[24] As a result, measurements with $c_i^{\text{sample}}=0$ are defined as aliased measurements, while those with $c_i^{\text{sample}}=1$ are defined as nonaliased measurements. All measurements with $1 > c_i^{\text{sample}} > 0$ are defined as partially aliased measurements.[9,10] A simple ratio model was employed to make it easy for a minimally trained operator to interpret the graphical representation of c_i^{sample}. The metric c_i^{sample} is a neighborhood-based metric because it assumes a complete neighborhood in which to find d_i^{far}, so its quality can be assessed using c_i^{enc}. Fiocco *et al.*[20] had previously defined a sampling quality metric based on the distance to the closest neighbor, while Sequeira *et al.*[2,18] applied a weighting factor to the average distance of the points in a measurement's neighborhood to obtain a quality metric. Neither approach took into account measurement uncertainty as part of the metric. Moreover, testing the distance to the closest neighbor, or even that average distance, does not ensure that all neighbors are close to the measurement.

2.8 *Total Quality Assessment*

A recent survey[1] of laser range scanner quality metrics identified two methods that have been employed for total quality assessments: weighted summation and product of binary pass/fails. A composite approach is used in this work in which all of the quality metrics presented in this section are divided into either exclusive quality metrics or augmenting quality metrics. Exclusive quality metrics are those that must all be acceptable ($c_i^{\text{metric}} > 0$) for the total quality of the measurement to be considered acceptable, while augmenting quality metrics are not critical for measurement acceptability, but should contribute to the total measurement quality assessment.[9,10] The total within-scan quality metric c_i^{total} is obtained using

$$c_i^{\text{total}} = c_i^{\text{excl}}[w_{\text{aug}}(c_i^{\text{aug}} - 1) + 1], \tag{15}$$

where $c_i^{\text{aug}} \in [0,1]$ is the weighted summation of the augmenting quality metrics, $c_i^{\text{excl}} \in [0,1]$ is the product of the exclusive quality metrics, and $w_{\text{aug}} \in [0,1]$ is the weighting factor applied to c_i^{aug}.

The exclusive quality metric is the product of those quality metrics that define the bounds of the scannable region. Only measurements with acceptable reflectivity, resolvability, orientation, return, and range quality are within the scannable region, so c_i^{excl} takes the form

$$c_i^{\text{excl}} = c_i^{\text{ref}} c_i^{\text{res}} c_i^{\text{orient}} c_i^{\text{return}} c_i^{\text{range}}. \tag{16}$$

The remaining metrics are combined to form c_i^{aug}, each of which is weighted based on how much they should influence the total quality assessment. The metric c_i^{aug} is found by

$$c_i^{\text{aug}} = \frac{w_{\text{plane}} c_i^{\text{plane}} + w_{\text{enc}} c_i^{\text{enc}} + w_{\text{blur}} c_i^{\text{blur}} + w_{\text{sample}} c_i^{\text{sample}} + w_{\text{out}} c_i^{\text{out}}}{w_{\text{plane}} + w_{\text{enc}} + w_{\text{blur}} + w_{\text{sample}} + w_{\text{out}}}, \tag{17}$$

where $\{w_{\text{plane}}, w_{\text{enc}}, w_{\text{blur}}, w_{\text{sample}}, w_{\text{out}}\} \geqslant 0$ are the weighting factors applied to each metric. The planarity, enclosed, integration, sampling, and outlier quality of a measurement can be unacceptable and the measurement still remain within the scannable region; however, nonzero quality values indicate a preferred (and therefore higher quality) measurement, so they must be included in the total quality assessment.

3 Adaptive Scanning

The metrics presented in Sec. 2 were used as part of an adaptive scanning method. This method starts with a Delaunay facet map of a low-density anchor scan covering the total field of view. An individual quality assessment is then performed using the metrics presented in Sec. 2, the results of which are used to divide the facet map into three regions based on the likelihood of obtaining additional useful and nonredundant data about the surface being scanned from

that viewpoint. Facets in which all vertices are nonreturn measurements or out-of-range measurements are combined to form the unscannable region. Facets in which all vertices are planar measurements are combined to initialize the complete region, then the remaining facets are used to initialize the rescan region. Facets in the complete region are transferred to the rescan region if:

- they contain reflectivity discontinuities with edge height ΔE_i^{ref} greater than the reflectivity threshold $E_{\text{threshold}}^{\text{ref}}$
- at least one vertex is a measurement with $c_i^{\text{out}} < c_{\text{threshold}}^{\text{out}}$, where $c_{\text{threshold}}^{\text{out}}$ is a threshold value
- at least one vertex is a nonreturn measurement
- at least one vertex is an angled measurement
- at least one vertex is an unresolvable measurement

after region initialization. The ΔE_i^{ref} term is the maximum difference in return signal intensity between $\mathbf{p}_i$ and any of its neighbors.

A series of small, high-density subscans is generated to completely cover the rescan region while minimizing the number of subscans performed. Each subscan is automatically generated with an intersample separation θ_{sep} that maximizes the likelihood of achieving Δx while minimizing the number of subscans obtained. The intersample separation is defined by

$$\theta_{\text{sep}} = \min_{i=1}^{N} \{\theta_i^{\Delta x} - \theta_i^{\text{err}}\}, \tag{18}$$

where

$$\theta_i^{\Delta x} = \tan^{-1}\left[\frac{\frac{\Delta x}{2}\cos(\gamma_i)}{R_i + \frac{\Delta x}{2}\sin(\gamma_i)}\right] \tag{19}$$

is the rotational distance. The subscans are initially generated using a grid pattern that completely covers the rescan region, then are moved using an iterative procedure to eliminate redundant scans and minimize coverage of the unscannable region while ensuring complete rescan region coverage. A second series of subscans is then performed for facets that were not covered by the previous set of subscans, or have at least one nonplanar vertex consisting of an aliased measurement after the first series of subscans have been merged into the anchor scan to form a composite range image. The merge method is based on the total quality of each measurement and is described in Sec. 3.1. The second series of subscans are then merged into the composite range image, a new individual quality assessment is performed for the points in the composite range image, and a total quality assessment is performed for the composite range image.[9,10] The total quality map can then be used to perform view planning, a topic beyond the scope of this work.

3.1 *Quality-Based Measurement Merger*

A composite range image (CRI) was initialized with all measurements from the anchor scan. All measurements from each subscan were then extracted and the rotational distance between each subscan measurement and the rotationally closest (corresponding) measurement in the composite range image was determined. Subscan measurements in which the rotational distance was less than the chi-squared difference between measurements[25,26] were then selected to be merged using a quality-weighted modified Kalman minimum variance (weighted-MKMV) estimation method.

The weighted-MKMV method involves weighting the covariance matrices with the total within-scan quality associated with the measurement. Given a measurement $\mathbf{p}_{i,\text{CRI}}$ in the composite range image with total within-scan quality $c_{i,\text{CRI}}^{\text{total}}$ and its corresponding subscan measurement $\mathbf{p}_{i,\text{sub}}$ with total within-scan quality $c_{i,\text{sub}}^{\text{total}}$ the measurement $\mathbf{p}_{i,\text{CRI}}$ is updated using

$$\mathbf{p}_{i,\text{CRI}} = (W_i^{-1} c_{i,\text{CRI}}^{\text{total}} \Sigma_{i,\text{CRI}}^{-1})\mathbf{p}_{i,\text{CRI}} + (W_i^{-1} c_{i,\text{sub}}^{\text{total}} \Sigma_{i,\text{sub}}^{-1})\mathbf{p}_{i,\text{sub}}, \tag{20}$$

where

$$W_i = c_{i,\text{CRI}}^{\text{total}} \Sigma_{i,\text{CRI}}^{-1} + c_{i,\text{sub}}^{\text{total}} \Sigma_{i,\text{sub}}^{-1} \tag{21}$$

is the weighting matrix. In these equations, $\Sigma_{i,\text{sub}}$ is the covariance of $\mathbf{p}_{i,\text{sub}}$ and $\Sigma_{i,\text{CRI}}$ is the covariance of measurement $\mathbf{p}_{i,\text{CRI}}$, and $c_{i,\text{CRI}}^{\text{total}}$ and $c_{i,\text{sub}}^{\text{total}}$ are scalar. The covariance matrix estimate is updated using

$$\Sigma_{i,\text{CRI}} = \frac{1}{c_{i,\text{CRI}}^{\text{total}} + c_{i,\text{sub}}^{\text{total}}} W_i^{-1}, \tag{22}$$

which weights the covariance matrix elements toward the higher quality measurement.[9,10]

The process of updating the composite range image with each subscan proceeds as follows:

- If $c_{i,\text{CRI}}^{\text{total}} > 0$ and $c_{i,\text{sub}}^{\text{total}} > 0$, then the weighted-MKMV method is used.
- If $c_{i,\text{CRI}}^{\text{total}} = 0$ and $c_{\text{sub},i}^{\text{total}} = 0$, then $\mathbf{p}_{i,\text{CRI}}$ and $\Sigma_{i,\text{CRI}}$ are updated using the MKMV estimator method.[23]
- If $c_{i,\text{CRI}}^{\text{total}} > 0$ and $c_{i,\text{sub}}^{\text{total}} = 0$, then $\mathbf{p}_{i,\text{CRI}}$ and its associated covariance matrix $\Sigma_{i,\text{CRI}}$ are unchanged.
- If $c_{i,\text{CRI}}^{\text{total}} = 0$ and $c_{i,\text{sub}}^{\text{total}} > 0$, then $\mathbf{p}_{i,\text{CRI}}$ is assigned the value of $\mathbf{p}_{i,\text{sub}}$ and $\Sigma_{i,\text{CRI}}$ is replaced with $\Sigma_{i,\text{sub}}$, the covariance matrix associated with $\mathbf{p}_{i,\text{sub}}$.

Finally, the total within-scan quality is updated such that

$$c_{i,\text{CRI}}^{\text{total}} = w_{i,\text{CRI}} c_{i,\text{CRI}}^{\text{total}} + w_{i,\text{sub}} c_{i,\text{sub}}^{\text{total}}, \tag{23}$$

where

$$w_{i,\text{CRI}} = \frac{c_{i,\text{CRI}}^{\text{total}}}{w_i \sigma(\mathbf{p}_{i,\text{sub}} | \mathbf{p}_{i,\text{CRI}} \Sigma_{i,\text{CRI}})^2}, \tag{24}$$

and

$$w_{i,\text{subscan}} = \frac{c_{i,\text{sub}}^{\text{total}}}{w_i \sigma(\mathbf{p}_{i,\text{CRI}} | \mathbf{p}_{i,\text{CRI}}, \Sigma_{i,\text{sub}})^2} \tag{25}$$

are the weighting factors. The total weight w_i is found using

$$w_i = \frac{c_{i,\mathrm{CRI}}^{\mathrm{total}}}{\sigma(\mathbf{p}_{i,\mathrm{sub}}|\mathbf{p}_{i,\mathrm{CRI}},\Sigma_{i,\mathrm{CRI}})^2} + \frac{c_{i,\mathrm{sub}}^{\mathrm{total}}}{\sigma(\mathbf{p}_{i,\mathrm{CRI}}|\mathbf{p}_{i,\mathrm{CRI}},\Sigma_{i,\mathrm{sub}})^2}, \quad (26)$$

where both the denominator terms are unit variance terms. For example, $\sigma(\mathbf{p}_{i,\mathrm{sub}}|\mathbf{p}_{i,\mathrm{CRI}},\Sigma_{i,\mathrm{CRI}})^2$ represents the variance along the line from $\mathbf{p}_{i,\mathrm{CRI}}$ to $\mathbf{p}_{i,\mathrm{sub}}$, given that $\Sigma_{i,\mathrm{CRI}}$ is the covariance associated with $\mathbf{p}_{i,\mathrm{CRI}}$.[9,10] The scalar equivalent variance function is explained in Appendix B in Sec. 7. Once all scans have been merged into the composite range image, the quality-weighted covariance from Eq. (22) is retained for each measurement, but the total within-scan quality from Eq. (23) is discarded as no longer being required.

3.2 *Experimental Results*

For this experiment, all scans were performed using a prototype medium-range (1- to 10-m range) laser spot range scanner developed by the National Research Council of Canada. Data processing consisted of applying a 7×7 median filter to the anchor scan and a 25×25 median filter to each subscan to reduce measurement noise. The outlier threshold value was $c_{\mathrm{threshold}}^{\mathrm{out}}=0.5$, reflectivity discontinuities were detected using a 3×3 Sobel filter with edge threshold $E_{\mathrm{threshold}}^{\mathrm{ref}}=0.1$, the target surface resolution was $\Delta x=2$ mm, the maximum acceptable surface orientation was $\gamma_{\max}=\pi/4$, the range limits were $R_{\max}=4$ m and $R_{\min}=1$ m, and the reflectivity limits were $\rho_{\min}=0$ and $\rho_{\max}=2$. The anchor and subscans consisted of 256×256 element raster scans and were assumed to have a 14-element acceleration and deceleration region at the start and end of each scan line, in which measurement values would be zeroed by the laser range scanner control system. Individual quality assessment of the anchor scans used $N(\mathbf{p}_i)$, defined as the set of all eight measurements that surround $\mathbf{p}_i$. Individual quality assessment of the composite range image was based on $N(\mathbf{p}_i)$, defined as the set of all $\mathbf{p}_j \in N(\mathbf{p}_i)$ that share a single Delaunay edge. Determination of the optimal weighting factor values was not part of the study, so that total quality assessment of the composite range image used $w_{\mathrm{aug}}=0.5$ and $w_{\mathrm{plane}}=w_{\mathrm{enc}}=w_{\mathrm{blur}}=w_{\mathrm{alias}}=w_{\mathrm{out}}=0.2$. The effect of parallax was assumed to be negligible, so distance to the beam waist was assumed to be constant; specifically, $R_{\mathrm{spot}}(\theta,\phi_i)=1.40$ m.[9]

Figure 4 illustrates the adaptive scanning processing using one of the test surfaces. Figure 4(a) shows one of the test surfaces used during the course of this investigation. The large planar surface was used for calibration of the laser range scanner's uncertainty and reflectivity models, so it represents a near-ideal surface for scanning purposes. In front of the posterboard is a picture of four distributor caps, which is a planar surface that features reflectivity discontinuities. To the left of the planar surface is a large plastic planter with a spatially complex surface and an average surface normal that is highly oriented with respect to the line of sight of the scanner. The picture of distributor caps is located 1 cm in front of the posterboard, so it represents a source of range discontinuities, while the top and side of the posterboard represent a truncated surface in which the farther surface is beyond the range of the scanner.

The first step in the adaptive scanning process was to perform a low-density scan of the total field of view. The quality metrics described in Sec. 2 were computed for all measurements, and the quality assessment described in Sec. 3 was used to generate the region map shown in Fig. 4(b). The unscannable region is shown in white, the complete region in light gray, and the rescan region in dark gray.

The second step in the process was to generate a series of subscans to completely cover the rescan region while minimally covering the unscannable region as described in Sec. 3. Figure 4(c) shows the placement of the first series of subscans. Each dashed box in Fig. 4 represents the area expected to be covered by a scan, while the solid box represents the region within which usable measurements should be obtained.

The third step in the process was to remove from the region map the portions of the rescan region that had been completely covered by each subscan. The quality metrics described in Sec. 2 were then computed for all measurements in each subscan. Areas of each subscan that contained aliased measurements were added to the rescan region to form an undated region map. A second set of subscans was then performed to completely cover the updated rescan region while minimizing coverage of the unscannable region after the intersample distance was reduced to compensate for the degree of aliasing detected. Figure 4(d) shows the placement of the second series of subscans. As a result, the subscans in Fig. 4(d) are smaller than those in Fig. 4(c).

Table 1 shows the results of five experiments using the adaptive scanning method. Scan time efficiency is the total scan plus processing time using the adaptive scanning approach divided by the total scan plus processing time for a high-density scan of the total field of view. The scan plus processing time for a high-density scan is the same for all experiments because the same field of view is used in all cases. Sampling efficiency was similarly calculated by dividing the number of measurements in the composite range image by the number that would be in a high-density scan of the total field of view. The size of the total field of view and sampling density used in a high-density scan is the same in all experiments, so the number of measurements collected is the same. In all cases, scan time and sampling efficiencies were less than 25%, where smaller efficiency values are better. For comparison, an efficiency value of 100% would indicate a process no more efficient than a high-density scan of the total field of view. These results show that an adaptive scanning approach can take less time and generate fewer measurements than simply performing a high-density scan of the total field of view. But the degree of improvement depends on the surface complexity, so it will be highly scene-dependent. The last row in Table 1 shows a portion of the final model from each experiment after merging all anchor and subscans using the adaptive scanning approach.

4 Discussion

The experimental results indicate that a considerable reduction in scanning time and number of measurements is possible; however, the cost of these reductions is also a reduction in final model accuracy compared to one generated from performing a high-density scan of the total field of view. For example, if all measurements in a region have a high planarity quality, this means that the level of nonpla-

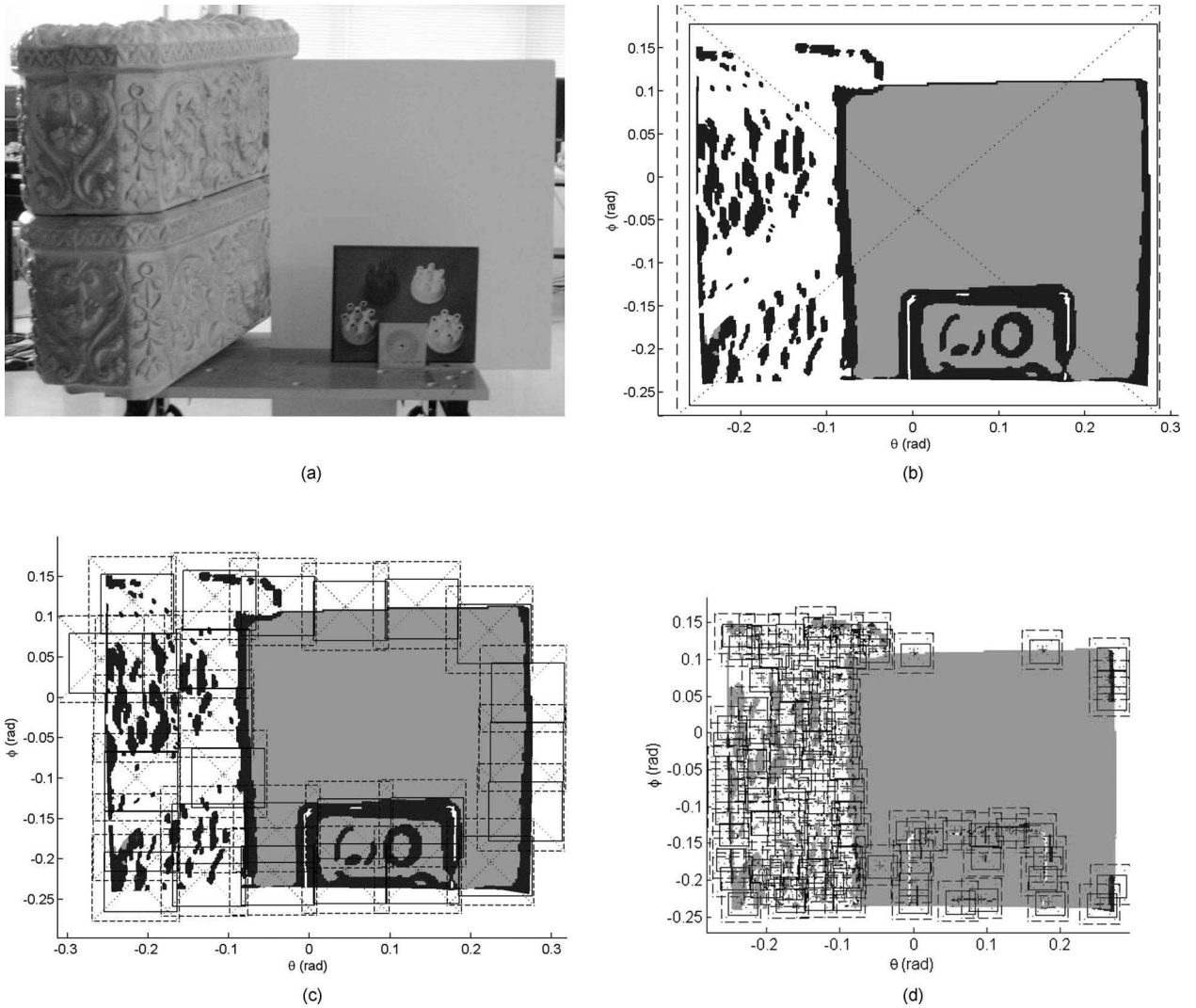

Fig. 4 Experiment used to illustrate the adaptive scanning technique. (a) Target object, (b) region map, (c) first set of subscans, and (d) second set of subscans.

narity based on a low-density scan is low, but using a low-density scan means that fine surface details will be missed. This approach, therefore, is only useful if fine model detail is not required, such as when generating a CAD model of a structure. The adaptive scanning approach represents a trade-off between final model quality and both scanning time and the size of the final model.

The quality metrics presented in this study were the result of a thorough assessment of the various parameters that can affect the quality of a measurement in a range image generated by a laser range scanner. In particular, the resolvability, blur, and sampling quality metrics arose from a study of the effect of spot size, shape, and motion on the quality of measurements in a range image. Blur and sampling quality metrics represented a way to weight measurement quality toward measurements obtained from subscans (that have higher blur and sampling quality) over the anchor scan (that have lower blur and sampling quality) without simply discarding the anchor scan data within subscanned regions. Similarly, planarity, outlier, and enclosed quality of measurements from a region can vary depending on whether they were generated from the anchor scan or one of the subscans because they are neighborhood-based metrics. Once again, it was important to include them when merging anchor scan and subscan measurements so that their effect would be considered when weighting spatially close measurements. All quality metrics were used when generating the total measurement quality because the total quality of a measurement should represent the contribution of all quality parameters.

In Sec. 1 it was proposed that the adaptive scanning approach could be used as part of a view-planning strategy. Specifically, resolvability, range, and orientation quality metrics can be used to suggest new scanner positions that might result in an improvement in the quality of measurements obtained. Experiments were performed to explore the use of quality metrics in view planning. An anchor scan was obtained from a randomly selected viewpoint, then a predictive quality assessment was performed in which a virtual version of the scanner was moved in a direction that maximized the resolvability, range, and orientation quality metrics. The scanner was then moved to the position indi-

Table 1 Scan time and sampling efficiencies versus total field of view. Total=anchor scan time +total scan time for all subscans+processing time for all scans. Scan time efficiency is versus total field of view scan+processing time=456.68 min, which is the same for all experiments. Sampling efficiency is versus number of samples from the total field of view scan=25,396,875 measurements, which is the same for all experiments.

	Fiberglass Head	Wall Section	Pumpkin Statue	Lawn Ornament	Planter
		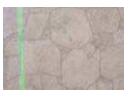			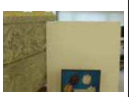
Total (min)*	58.54	106.35	67.40	108.60	101.80
Scan Time Efficiency†	12.8%	23.3%	14.8%	23.8%	22.3%
Measurements	4,128,768	7,602,176	4,980,736	8,126,464	7,536,640
Sampling Efficiency‡	16.3%	29.9%	19.6%	32.0%	37.4%
		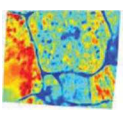		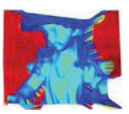	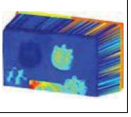

*Total = anchor scan time + total scan time for all subscans + processing time for all scans

†Scan Time Efficiency is versus total field of view scan + processing time = 456.68 minutes, which is the same for all experiments.

‡Sampling Efficiency is versus number of samples from the total field of view scan = 25,396,875 measurements, which is the same for all experiments.

cated by the predictive quality assessment and the process was repeated. In experiments using all five test surfaces, an optimal location was obtained after no more than three iterations, demonstrating that quality metrics could be used to successfully test alternative viewpoints prior to moving the scanner. An example of the predictive quality assessment approach is shown in Fig. 5.[9] In a view-planning strategy, a predictive quality assessment would be performed only for regions of the model with low orientation, resolvability, or range quality, while minimizing coverage of model regions that already have high total quality.

5 Conclusions

The adaptive scanning method presented can significantly reduce both the total time spent scanning the surface and the total number of samples acquired to generate a range image from a single viewpoint. Experiments show that this method can take approximately 24% of the time and generate approximately 37% of the measurements compared to a high-density scan of the total field of view. Six new quality metrics are developed for the adaptive scanning method: return, enclosed, outlier, planarity, resolvability, and blur. The outlier quality metric is used to identify areas in which measurements were highly variable, such as near spatial and intensity discontinuities. The planarity quality metric is used to identify areas that could be represented as a planar surface, and so would require few measurements to characterize. The return quality metric is used to identify areas of the initial scan, from which it is unlikely that useful measurements could be obtained. Four improved quality metrics are also presented: orientation, reflectivity, range, and sampling. The sampling quality metric is used to establish an upper bound on the sample density to ensure that the sampling density is sufficiently high to capture surface details at the target resolution where necessary. The reflectivity, resolvability, orientation, return, and range quality metrics are used to define the boundaries of the scannable region for a given viewpoint. All metrics are combined into a total quality metric, which is then used to merge measurements from all scans that are statistically close based on their quality-weighted covariance into a single composite range image. The resulting composite range image contains fewer measurements than would result from simply combining multiple scans, and the measurement covariances accurately reflect the reduction in measurement uncertainty resulting from the quality-weighted averaging of spatially close measurements.

Appendix A: Axial Dimensions in the Midfield

The surface dimensions of the region illuminated by the laser beam can be obtained for midfield measurements if the surface is assumed to be strictly planar within the beam footprint. Consider Fig. 2(a), which illustrates the intersection of the laser beam with a surface angled ρ_i with respect to the laser path. The spot radius $w(\xi)$ a distance ξ from the beam waist can be found by

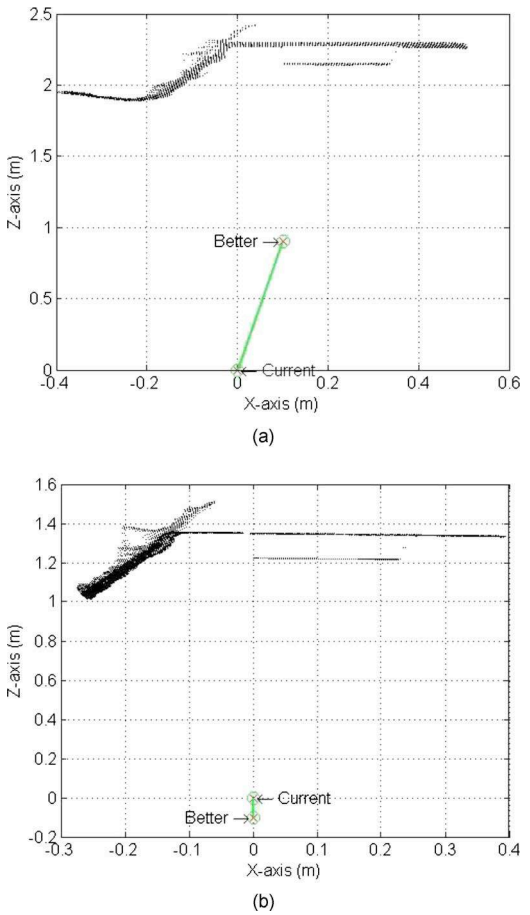

Fig. 5 Experiment to explore view planning. (a) Initial viewpoint and next best viewpoint based on predictive quality assessment. (b) Second viewpoint and predicted next best viewpoint. A predictive quality assessment of the third viewpoint indicated no other viewpoint will maximize orientation, resolvability, and range quality metrics.

$$w(\zeta) = w(0)\sqrt{1+\left(\frac{\zeta}{\zeta_0}\right)^2}, \tag{27}$$

where $w(0)$ is the radius of the beam waist and ξ_0 is the depth of focus.[13] Equation (27) can be rewritten as

$$\zeta_0^2 w(\zeta)^2 = \zeta_0^2 w_0^2 + \zeta^2 w_0^2, \tag{28}$$

where we have used $w_0 = w(0)$ to simplify the equation.

Figure 6 illustrates the cross section of the plane intersecting the laser beam. The plane intersects the center of the beam at a distance ξ_1 from the beam waist, and intersects the $1/e^2$ boundary at ξ_2 from the beam waist. We use $w_1 = w(\xi_1)$ and $w_2 = w(\xi_2)$ to represent the widths of the beam at a distance ξ_1 and ξ_2, respectively. The term ξ_1 also represents the distance between the beam waist and the spatial location of the measurement generated by the reflected beam footprint, so it can be easily obtained. Similarly, w_1 represents the spot radius corresponding to the measurement $\hat{\mathbf{p}}$, so it is also easily obtained. Finally, ρ is estimated from the surface normal $\vec{n}_i$ of the neighborhood regression plane through $\hat{\mathbf{p}}$. What remains is to find d, the surface distance between the peak and edge of the beam footprint.

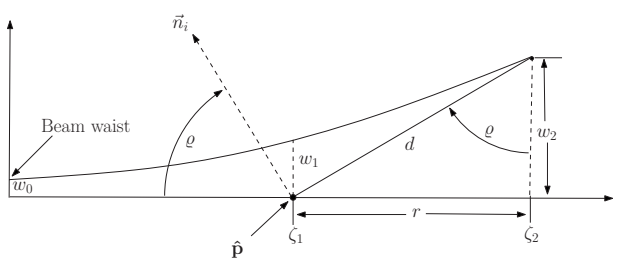

Fig. 6 Beam-surface intersection.

The terms ξ_2 and w_2 are unknown and need to be eliminated. From Fig. 6, we see that

$$\zeta_2 = \zeta_1 + r, \tag{29}$$

where

$$r = d\sin(\rho), \tag{30}$$

so

$$\zeta_2 = \zeta_1 + d\sin(\rho), \tag{31}$$

in which all the terms in the right-hand side are known. Similarly,

$$w_2 = d\cos(\rho) \tag{32}$$

is expressed in terms of d and ρ, which are also known. Substituting Eqs. (31) and (32) into Eq. (28) results in

$$\zeta_0^2 d^2\cos^2(\rho) = \zeta_0^2 w_0^2 + w_0^2[\zeta_1 + d\sin(\rho)]^2. \tag{33}$$

Equation (33) can be expanded in terms of d into an equation of the form

$$d^2 K_1 + dK_2 + K_3 = 0, \tag{34}$$

where

$$K_1 = [w_0\sin(\rho)]^2 - [\zeta_0\cos(\rho)]^2, \tag{35}$$

$$K_2 = 2\zeta_1 w_0^2\sin(\rho), \tag{36}$$

and

$$K_3 = [w_0\zeta_0]^2 + [w_0\zeta_1]^2. \tag{37}$$

Equation (34) can now be solved using a quadratic equation, generating two possible values of d. These values are the lengths of the long and short axes, representing the cross section of the intersection of the surface with the $1/e^2$ boundary. Specifically,

$$\{d_{\min}, d_{\max}\} = \left|\frac{-K_2 \pm \sqrt{(K_2)^2 - 4K_1K_3}}{2K_1}\right|. \tag{38}$$

Equation (28) is symmetrical about the beam waist, so this approach holds throughout the midfield regardless of whether the surface is closer to or farther from the laser with respect to the beam waist. As $\rho \to 0$, $d_{\max} \to d_{\min}$ and $d_{\text{length}} = d_{\max} + d_{\min} \to d_{\text{width}} = 2w_1$, where d_{length} and d_{width} are

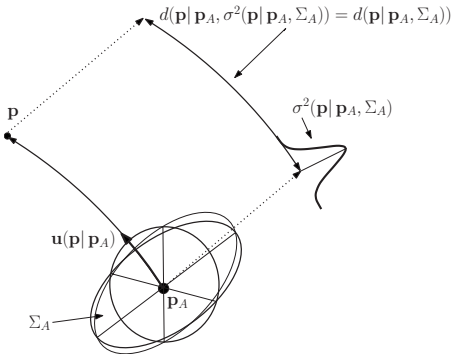

Fig. 7 The scalar equivalent variance (SEV) $\sigma^2(\mathbf{p}|\mathbf{p}_A,\Sigma_A)$ is the variance along the shortest line segment in spherical space to $\mathbf{p}$ given starting point $\mathbf{p}_A$ with covariance Σ_A. $d[\mathbf{p}|\mathbf{p},\sigma^2(\mathbf{p}|\mathbf{p}_A,\Sigma_A)]$ is the Mahalanobis distance to $\mathbf{p}$ given starting point $\mathbf{p}_A$ and scalar equivalent variance $\sigma^2(\mathbf{p}|\mathbf{p}_A,\Sigma_A)$.

the length and width of the ovoid beam footprint, respectively.

Appendix B: Scalar-Equivalent Variance

The scalar variance equivalent form is relatively easy to conceptualize when all the elements of the local surface points use the same units of measure; however, in the spherical coordinate system, the rotational and radial components have different units of measure. The Mahalanobis distance is a unitless quantity, so the elements of the points used to calculate the Mahalanobis distance can be treated as unitless, and the scalar equivalent variance becomes a weighting factor for the unitless Euclidean distance between two points. It can be defined using

$$d^2(\mathbf{p}|\mathbf{p}_A,\Sigma_A) = (\mathbf{p}_A-\mathbf{p})^T\Sigma_A^{-1}(\mathbf{p}_A-\mathbf{p}), \tag{39}$$

where Σ_A is the covariance matrix associated with surface point $\mathbf{p}_A$, and $\sqrt{d^2(\mathbf{p}|\mathbf{p}_A,\Sigma_A)}$ is the distance to some point $\mathbf{p}$ in the environment given a measurement $\mathbf{p}_A$ with covariance Σ_A. The $d^2(\mathbf{p}|\mathbf{p}_A,\Sigma_A)$ term has a χ^2 distribution, so $d^2(\mathbf{p}|\mathbf{p}_A,\Sigma_A) < \chi^2(d_f,\alpha)$, where d_f is the number of degrees of freedom and α is the probability level, can be used to test whether measurement $\mathbf{p}$ is sufficiently close to the surface point $\mathbf{p}_A$ that it is likely to arise from the surface at probability level α.[25,26]

The calculation of the Mahalanobis distance can be simplified by representing the covariance matrix Σ_A as a unitless scalar equivalent variance function $\sigma^2(\mathbf{p}|\mathbf{p}_A,\Sigma_A)$ along a unit vector $\mathbf{u}(\mathbf{p}|\mathbf{p}_A)$. The scalar equivalent variance is the scalar variance at point $\mathbf{p}$ given a local surface point $\mathbf{p}_A$ with covariance Σ_A, and the unit vector is a vector oriented toward $\mathbf{p}$ given a local surface point $\mathbf{p}_A$. A graphical representation of the scalar equivalent variance can be seen in Fig. 7. Consider a line from $\mathbf{p}_A$ to some point in space $\mathbf{p}$ as shown in Figure 7. If the variance of a cross section of Σ_A along the shortest path in spherical space from $\mathbf{p}_A$ to $\mathbf{p}$ can be represented by a scalar variance $\sigma^2(\mathbf{p}|\mathbf{p}_A,\Sigma_A)$, then Eq. (39) can be rewritten as

$$d^2(\mathbf{p}|\mathbf{p}_A,\sigma^2(\mathbf{p}|\mathbf{p}_A,\Sigma_A)) = \frac{\|\mathbf{p}_A-\mathbf{p}\|_G^2}{\sigma^2(\mathbf{p}|\mathbf{p}_A,\Sigma_A)}, \tag{40}$$

where $\sigma^2(\mathbf{p}|\mathbf{p}_A,\Sigma_A)$ is the variance of the Gaussian distribution around $\mathbf{p}_A$ along a line segment in spherical space from $\mathbf{p}_A$ to $\mathbf{p}$. The numerator term $\|\mathbf{p}_A-\mathbf{p}\|_G^2$ is the Euclidean distance between $\mathbf{p}_A$ and $\mathbf{p}$, where $\mathbf{p}_A,\mathbf{p}\in G$ and $G\subset\mathbb{R}^3$ is a bounded region in which: the rotational components are bounded such that $\theta \leqslant \min\{\theta_{\max},\pi\}$ and $\theta > \max\{\theta_{\min},-\pi\}$, where $\theta_{\max}$ and $\theta_{\max}$ are the bounds of the total field of view of the scanner along the θ axis, and $\phi \leqslant \min\{\phi_{\max},\pi\}$ and $\phi > \max\{\phi_{\min},-\pi\}$, where $\phi_{\max}$ and $\phi_{\max}$ are the bounds of the total field of view of the scanner along the ϕ axis. This avoids the problem of two radial measurement values representing the same spatial point. Also, the radial component is restricted to being larger than zero, so that no point is allowed to exist at the origin; that is $R > R_{\min} > 0$.

These restrictions define the boundaries of a region G in the Cartesian space $\mathbb{R}^3$. Points within this space can be represented in either spherical or Cartesian coordinates.

Both Eqs. (39) and (40) express the same distance metric so they can be combined such that

$$\frac{\|\mathbf{p}_A-\mathbf{p}\|_G^2}{\sigma^2(\mathbf{p}|\mathbf{p}_A,\Sigma_A)} = (\mathbf{p}_A-\mathbf{p})^T\Sigma_A^{-1}(\mathbf{p}_A-\mathbf{p}). \tag{41}$$

Rearranging the terms results in

$$\frac{1}{\sigma^2(\mathbf{p}|\mathbf{p}_A,\Sigma_A)} = \frac{(\mathbf{p}_A-\mathbf{p})^T}{\|\mathbf{p}_A-\mathbf{p}\|_G}\Sigma_A^{-1}\frac{(\mathbf{p}_A-\mathbf{p})}{\|\mathbf{p}_A-\mathbf{p}\|_G}, \tag{42}$$

in which the first and last terms are unit vectors. These terms can be replaced with a single unit vector $\mathbf{u}(\mathbf{p}|\mathbf{p}_A)$. Equation (42) can be rewritten as

$$\sigma^2(\mathbf{p}|\mathbf{p}_A,\Sigma_A) = \frac{1}{\mathbf{u}^T(\mathbf{p}|\mathbf{p}_A)\Sigma_A^{-1}\mathbf{u}(\mathbf{p}|\mathbf{p}_A)}, \tag{43}$$

where

$$\mathbf{u}(\mathbf{p}|\mathbf{p}_A) = \frac{\mathbf{p}_A-\mathbf{p}}{\|\mathbf{p}_A-\mathbf{p}\|_G}. \tag{44}$$

Intuitively, Eq. (43) represents the variance in the direction indicated by the unit vector when the unit vector is applied to the covariance matrix. Now, given a known scalar equivalent variance, the Mahalanobis distance can be calculated using Eq. (40).

References

1. D. MacKinnon, V. Aitken, and F. Blais, "Review of measurement quality metrics for range imaging," *J. Electron. Imaging* **17**, 033003 (2008).
2. V. Sequeira, K. Ng, E. Wolfart, J. G. M. Gonçalves, and D. Hogg, "Automated reconstruction of 3D models from real environments," *ISPRS J. Photogramm. Remote Sens.* **54**, 1–22 (1999).
3. M. Callieri, A. Fasano, G. Impoco, P. Cignoni, R. Scopigno, G. Parrini, and G. Biagini, "RoboScan: an automatic system for accurate and unattended 3D scanning," in *Proc. 2nd Intl. Symp. 3D Data Process. Visual. Transmission*, pp. 805–812, IEEE, Piscataway, NJ (2004).
4. W. Scott, G. Roth, and J. F. Rivest, "View planning for multi-stage object reconstruction," in *Proc. Intl. Conf. Vision Interface*, pp. 64–71, CIPPRS/IAPR (2001), http://www.cipprs.org/vi2001/.
5. M. Adams, "Lidar design, use, and calibration concepts for correct environmental detection," *IEEE Trans. Rob. Autom.* **16**, 753–761 (2000).
6. J. Hancock, D. Langer, M. Hebert, R. Sullivan, D. Ingimarson, E. Hoffman, M. Mettenleiter, and C. Froehlich, "Active laser radar for

high-performance measurements," in *Proc. IEEE Intl. Conf. Robotics Auto.*, Vol. 2, pp. 1465–1470, IEEE, Piscataway, NJ (1998).
7. J. A. Beraldin, M. Picard, S. El-Hakim, G. Godin, L. Borgeat, F. Blais, E. Paquet, M. Rioux, V. Valzano, and A. Bandiera, "Virtual reconstruction of heritage sites: opportunities and challenges created by 3D technologies," in *Proc. Intl. Workshop Recording, Model. Visual. Cultural Heritage*, pp. 141–156, Taylor & Francis, Leiden, The Netherlands (2005).
8. A. Johnson, R. Hoffman, J. Osborn, and M. Hebert, "A system for semi-automatic modeling of complex environments," in *Proc. 3rd Intl. Conf. Recent Advances 3-D Digital Imag. Model*, pp. 213–220, IEEE, Piscataway, NJ (1997).
9. D. MacKinnon, "Adaptive laser range scanning using quality metrics," PhD Dissertation, Carleton University, Canada (2008).
10. D. MacKinnon, J. A. Beraldin, L. Cournoyer, and F. Blais, "Evaluating laser range scanner lateral resolution in 3D metrology," *Proc. SPIE* **7239**, 72390p (2009).
11. W. Mendenhall, *Mathematical Statistics with Applications*, 3rd ed., PWS Publishers, Boston, MA (1986).
12. I. Stamos and P. K. Allen, "3-D model construction using range and image data," in *Proc. IEEE Conf. Computer Vision Patt. Recog.*, Vol. 1, pp. 531–536, IEEE, Piscataway, NJ (2000).
13. B. Chu, *Laser Light Scattering Basic Principles and Practice*, 2nd ed., pp. 156–160, Academic Press, San Diego, CA, (1991).
14. H. T. Yura, "Atmospheric turbulence induced laser beam spread," *Appl. Opt.* **10**, 2771–2773 (1971).
15. R. E. Walker and J. W. McLean, "Lidar equations for turbid media with pulse stretching," *Appl. Opt.* **38**, 2384–2397 (1999).
16. R. Baribeau and M. Rioux, "Influence of speckle on laser range finders," *Appl. Opt.* **30**, 2873–2978 (1991).
17. R. Baribeau and M. Rioux, "Centroid fluctuations of speckled targets," *Appl. Opt.* **30**, 3752–3755 (1991).
18. V. Sequeira, K. Ng, E. Wolfart, J. G. Goncalves, and D. Hogg, "Automated 3D reconstruction of interiors with multiple scan-views," *Proc. SPIE* **3641**, 106–117 (1998).
19. B. L. Curless, "New methods for surface reconstruction from range images," PhD Thesis, Stanford University, CA (1997).
20. M. Fiocco, G. Boström, J. Gonçalves, and V. Sequeira, "Multisensor fusion for volumetric reconstruction of large outdoor areas," in *Proc. IEEE Fifth Intl. Conf. 3-D Digital Imaging Model.*, pp. 47–54, IEEE, Piscataway, NJ (2005).
21. M. Soucy, A. Croteau, and D. Laurendeau, "A multi-resolution surface model for compact representation of range images," in *Proc. IEEE Intl. Conf. Robotics Auto.* Vol. 2, pp. 1701–1706, IEEE, Piscataway, NJ (1992).
22. G. Turk and M. Levoy, "Zippered polygon meshes from range images," in *Proc. SIGGraph*, pp. 311–318, ACM, New York (1994).
23. M. Rutishauser, M. Stricker, and M. Trobina, "Merging range images of arbitrarily shaped objects," in *Proc. Conf. Computer Vision Patt. Recog. (CVPR'94)*, pp. 573–580, IEEE Computer Society, Washington, DC (1994).
24. A. V. Oppenheim and R. W. Schafer, *Discrete Signal Processing*, 2nd ed., Prentice-Hall Signal Processing, Prentice-Hall, Englewood Cliff, NJ (1999).
25. J. Neira and J. D. Tardós, "Data association in stochastic mapping using the joint compatibility test," *IEEE Trans. Rob. Autom.* **17**, 890–897 (2001).
26. I. J. Cox, "A review of statistical data association techniques for motion correspondence," *Int. J. Comput. Vis.* **10**(1), 53–66 (1993).

David MacKinnon holds a BSc (1990) in mathematics from the University of Prince Edward Island (PEI), a BSc (2001) in electrical and computer engineering from the University of New Brunswick, and both an MASc (2003) and PhD (2008) in electrical engineering from Carleton University, Ottawa. He is currently a research associate with the National Research Council Canada's Institute for Information Technology, working in the area of measurement standards in 3-D metrology. Between 1991 and 1998, he worked as a statistician, first with the PEI Food Technology Centre, then with the UPEI Clinical Research Centre. He is currently an engineer-in-training with the Association of Professional Engineers and Geoscientists of New Brunswick.

François Blais is a principal research officer and group leader of visual information technology at the National Research Council Canada's Institute for Information Technology. He received his BSc and MSc in electrical engineering from Laval University, Quebec City. Since 1984, his research has resulted in the development of a number of innovative 3-D sensing technologies licensed to various industries and applications, including space and the in-orbit 3-D laser inspection of NASA's space shuttles. He led numerous research and development initiatives in 3-D and the scanning and modeling of important archeological sites and objects of art including the masterpiece Mona Lisa by Leonardo Da Vinci. He received several awards of excellence for his work and is very active on the international scene with scientific committees, more than 150 publications and patents, invited presentations, and tutorials.

Victor Aitken holds a BSc (1987) in electrical engineering and mathematics from the University of British Columbia, and the MEng (1991) and PhD (1995) degrees in electrical engineering from Carleton University, Ottawa. He is currently an associate professor and chair of the Department of Systems and Computer Engineering at Carleton University, Ottawa, and is a member of the Professional Engineers of Ontario. His research interests include control systems, state estimation, data and information fusion, redundancy, sliding mode systems, nonlinear systems, and vision, mapping, and localization for navigation and guidance of unmanned vehicle systems with applications in underground mining, landmine detection, and exploration.